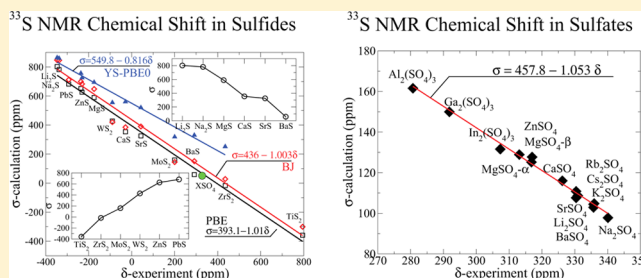


# Understanding of $^{33}\text{S}$ NMR Shielding in Inorganic Sulfides and Sulfates

Robert Laskowski<sup>\*,†</sup> and Peter Blaha<sup>‡</sup><sup>†</sup>Institute of High Performance Computing, A\*STAR, 1 Fusionopolis Way, #16-16, Connexis, Singapore 138632<sup>‡</sup>Institute of Materials Chemistry, Vienna University of Technology, Getreidemarkt 9/165-TC, A-1060 Vienna, Austria

**ABSTRACT:** Density functional theory (DFT) calculations of the magnetic shielding in solid state nuclear magnetic resonance (NMR) experiments provide an important contribution for the understanding of the experimentally observed chemical shifts. In this work we focus on the relation between atomic and orbital character of the valence and conduction band wave functions and the  $^{33}\text{S}$  NMR shielding in sulfides and sulfates. This allows us to understand the origin of the observed large (over 1000 ppm) variation of the chemical shifts measured at the sulfur nucleus. We show that the variation of the NMR chemical shifts in sulfides is mostly related to the presence of metal  $d$  states and their variation in the energy position within the conduction bands.



## INTRODUCTION

Nuclear magnetic resonance (NMR) measures the response of a material to an external magnetic field by detecting the transition energies related to the reorientation of the nuclear magnetic moment.<sup>1</sup> The external field induces an electric current in the sample, which according to Biot-Savart's law is the source of an induced magnetic field which partially screens the external field. The induced current and the screening field are very sensitive to the details of the electronic and atomic structure of a studied material. Therefore, NMR measurements became a useful and widely used characterization tool,<sup>2</sup> which provides valuable information on the local environment around the measured nuclei.

Usually the interpretation of the measured spectra is limited to an assignment of NMR shifts to a particular atomic site based on a comparison of the measured shifts with similar but simpler reference compounds. This process can be assisted by density functional theory (DFT) calculations of the corresponding magnetic shielding. However, such calculations may provide much more information than just the values of the shielding parameters. In a previous publication we have proposed a unique strategy to analyze the relation between electronic structure and NMR shielding and applied it to understand the origin of the variation of  $^{19}\text{F}$  NMR chemical shifts within a series of ionic fluoride compounds.<sup>3</sup> We showed that even in these highly ionic compounds the small mixing between metal and fluorine  $p$  character is the reason for the dependence of the magnetic response on the metal atom. The variation of the shielding is mostly related to the position of the metal- $d$  character in the conduction band.

In this work we perform a similar analysis on a series of inorganic sulfides and sulfates. The only NMR detectable sulfur isotope is  $^{33}\text{S}$ . It is a rather difficult nuclei to study by NMR due

to its low natural abundance (0.75%) and its small gyromagnetic ratio resulting in an absolute signal strength of only  $1.7 \times 10^{-5}$  of that for  $^1\text{H}$ . Moreover,  $^{33}\text{S}$  is a quadrupolar nucleus with spin  $I = 3/2$  and a quadrupole moment  $Q = -0.0678b$ , which causes considerable broadening of NMR spectra for compounds with nonspherical sulfur environment. These inherent difficulties are the reason why only relatively few  $^{33}\text{S}$  solid state NMR studies appeared in literature so far.<sup>4–14</sup> However, considering the rapid development of the experimental techniques, this will certainly change in the future. In any case, there are numerous compelling reasons to perform  $^{33}\text{S}$  NMR studies related to the fact that sulfur is a very common element present in many important biological or technological materials. Moreover, the sulfur NMR chemical shifts show significant sensitivity to the chemical environment, resulting in an over 1000 ppm wide range of shifts, which is, for instance, almost  $5\times$  larger than the variations observed in fluorides.

The paper is organized as follows. In the next section we briefly describe the fundamentals of our theoretical approach for computing the magnetic shielding, that are necessary for understanding the principles of our analysis. The following section contains a detailed analysis of the relation between the shielding at the sulfur nuclei and the details of the valence and conduction band wave functions, explaining the origin of the huge  $^{33}\text{S}$  NMR shift variations in sulfur compounds. The analysis is done separately for sulfides and sulfates due to their considerable different chemical characters. The last section concludes and summarizes the paper.

Received: September 23, 2014

Revised: December 9, 2014

Published: December 10, 2014

## THEORETICAL APPROACH

There are several ab initio methods described in literature for the calculation of NMR chemical shifts in molecules<sup>1,15</sup> and solids.<sup>16–21</sup> While the use of hybrid-DFT is quite common in molecular calculations using Gaussian basis sets, for solid state NMR they usually operate within the standard DFT<sup>22,23</sup> framework, but we have also used hybrid-DFT for the NMR shifts in highly ionic fluorides and oxides, although their performance was not overwhelming.<sup>24</sup> In the present work we use, in general, the PBE<sup>25</sup> functional, but when explicitly stated, we tested also the Becke-Johnson (BJ) potential,<sup>26</sup> which is an approximate exact-exchange potential and a hybrid-DFT functional<sup>27</sup> (YS-PBE0) with 25% of short-range Hartree–Fock exchange.

The formalism used in this work is based on a linear response approach<sup>16,18,19</sup> originally developed by Mauri, Pfrommer, and Louie (MPL).<sup>16</sup> However, it is adapted and implemented within the all-electron, full potential augmented plane wave method (APW).<sup>28,29</sup> The details of the implementation are described in our previous publications.<sup>30,31</sup> Formally our approach belongs to a set of gauge transformation methods, often referred as IGCV (individual gauge for core and valence) with a “ $d(r) = r$ ” gauge choice for the valence electrons.<sup>32</sup>

The NMR shielding tensor  $\vec{\sigma}$  is defined as a proportionality constant between the induced magnetic field  $\mathbf{B}_{\text{ind}}$  at the nucleus at site  $\mathbf{R}$  and the external uniform field  $\mathbf{B}$ :

$$\mathbf{B}_{\text{ind}}(\mathbf{R}) = -\vec{\sigma}(\mathbf{R})\mathbf{B} \quad (1)$$

Often only the isotropic shielding  $\sigma(\mathbf{R}) = \text{Tr}[\vec{\sigma}(\mathbf{R})]$  can be accessed experimentally. The actually measured quantity is the chemical shift  $\delta$ , which is the NMR isotropic shielding  $\sigma(\mathbf{R})$  with respect to a reference compound,  $\delta(\mathbf{R}) = \sigma_{\text{ref}} - \sigma(\mathbf{R})$ . An often quoted reference for <sup>33</sup>S is CS<sub>2</sub><sup>33</sup> and we have also done calculations for CS<sub>2</sub> using the experimentally determined crystal symmetry (*Cmca*) and lattice parameters (6.414, 5.579, 8.893 Å), but fully relaxing the internal atomic positions. The computed shielding is equal to 435.3 ppm, and this will be compared to the reference obtained by a linear fit of theoretical shielding versus experimental chemical shifts.

The induced field  $\mathbf{B}_{\text{ind}}$  is obtained by integrating the induced current  $\mathbf{j}_{\text{ind}}(\mathbf{r})$  (in atomic units, with  $c$  as the speed of light):

$$\mathbf{B}_{\text{ind}}(\mathbf{R}) = \frac{1}{c} \int d^3r \mathbf{j}_{\text{ind}}(\mathbf{r}) \times \frac{\mathbf{R} - \mathbf{r}}{|\mathbf{R} - \mathbf{r}|^3} \quad (2)$$

For nonmagnetic and insulating materials, only the orbital motion of the electrons contribute to  $\mathbf{j}_{\text{ind}}(\mathbf{r})$ . The current density is evaluated as an expectation value of the current operator:

$$\mathbf{J}(\mathbf{r}') = -\frac{\mathbf{p}|\mathbf{r}'\rangle\langle\mathbf{r}'| + |\mathbf{r}'\rangle\langle\mathbf{r}'|\mathbf{p}}{2} - \frac{\mathbf{B} \times \mathbf{r}'}{2c} |\mathbf{r}'\rangle\langle\mathbf{r}'| \quad (3)$$

The expression for the induced current involves only the first order terms with respect to the external field  $\mathbf{B}$ :

$$\mathbf{j}_{\text{ind}}(\mathbf{r}') = \sum_{\circ} [\langle \tilde{\Psi}_{\circ}^{(1)} | \mathbf{J}^{(0)}(\mathbf{r}') | \Psi_{\circ}^{(0)} \rangle + \langle \Psi_{\circ}^{(0)} | \mathbf{J}^{(0)}(\mathbf{r}') | \tilde{\Psi}_{\circ}^{(1)} \rangle + \langle \Psi_{\circ}^{(0)} | \mathbf{J}^{(1)}(\mathbf{r}') | \Psi_{\circ}^{(0)} \rangle] \quad (4)$$

where  $\Psi_{\circ}^{(0)}$  is an unperturbed Kohn–Sham (KS) occupied orbital,  $\mathbf{J}^{(0)}(\mathbf{r}')$  is the paramagnetic part of the current operator (the first term in eq 3),  $\mathbf{J}^{(1)}(\mathbf{r}')$  is the diamagnetic component of

the current operator (the second term in eq 3).  $\tilde{\Psi}_{\circ}^{(1)}$  is the first order perturbation of  $\Psi_{\circ}^{(0)}$  given by the standard formula:

$$|\tilde{\Psi}_{\circ}^{(1)}\rangle = \mathcal{G}(\epsilon_{\circ}) \mathbf{H}^{(1)} |\Psi_{\circ}^{(0)}\rangle \quad (5)$$

where  $\mathcal{G}(\epsilon) = \sum_{\epsilon} \left[ \frac{|\psi_{\epsilon}^{(0)}\rangle\langle\psi_{\epsilon}^{(0)}|}{\epsilon - \epsilon_{\circ}} \right]$ , and  $H^{(1)} = (1/2c)\mathbf{r} \times \mathbf{p} \cdot \mathbf{B}$  is the perturbation due to the external magnetic field in symmetric gauge. The last component in eq 4 is proportional to electron density which may lead to the gauge origin dependence of that expression. The generalized sum rule<sup>18</sup> allows to express this term using wave functions of the occupied bands:

$$\rho(\mathbf{r}') \mathbf{B} \times \mathbf{r}' = - \sum_{\circ} \langle \Psi_{\circ}^{(0)} | \frac{1}{i} [\mathbf{B} \times \mathbf{r}' \cdot \mathbf{r}, \mathbf{J}^{(0)}(\mathbf{r}')] | \Psi_{\circ}^{(0)} \rangle \quad (6)$$

Finally eq 4 can be cast into a simple form:

$$\mathbf{j}_{\text{ind}}(\mathbf{r}') = \frac{1}{c} \sum_{\circ} \text{Re}[\langle \Psi_{\circ}^{(0)} | \mathbf{J}^0(\mathbf{r}') | \tilde{\Psi}_{\circ}^{(1)} \rangle] \quad (7)$$

where  $\tilde{\Psi}_{\circ}^{(1)}$  is a perturbation of  $\Psi_{\circ}^{(0)}$  with “ $d(r) = r$ ” gauge choice:

$$|\tilde{\Psi}_{\circ}^{(1)}\rangle = \sum_{\epsilon} |\Psi_{\epsilon}^{(0)}\rangle \frac{\langle \Psi_{\epsilon}^{(0)} | [(\mathbf{r} - \mathbf{r}') \times \mathbf{p} \cdot \mathbf{B}] | \Psi_{\circ}^{(0)} \rangle}{\epsilon - \epsilon_{\circ}} \quad (8)$$

In the actual implementation the position operator  $\mathbf{r}$  is replaced by the limit  $\mathbf{r} \cdot \hat{\mathbf{u}}_i = \lim_{q \rightarrow 0} (1/2q)(e^{iq\hat{\mathbf{u}}_i \cdot \mathbf{r}} - e^{-iq\hat{\mathbf{u}}_i \cdot \mathbf{r}})$  to avoid the divergences for extended systems.

In the APW method the unit cell is decomposed into nonoverlapping atomic spheres and an interstitial region. The unperturbed wave functions as well as their first order perturbations are expressed using plane waves augmented with an atomic like angular momentum expansion inside the atomic spheres  $S_{\alpha}$ :

$$\Psi_{n,\mathbf{k}}(\mathbf{r}) = \begin{cases} \frac{1}{\sqrt{\Omega}} \sum_{\mathbf{G}} C_{\mathbf{G}}^{n,\mathbf{k}} e^{i(\mathbf{G}+\mathbf{k})\cdot\mathbf{r}}, & \mathbf{r} \in I \\ \sum_{lm} W_{lm}^{n,\alpha,\mathbf{k}}(r) Y_{lm}(\hat{r}), & \mathbf{r} \in S_{\alpha} \end{cases} \quad (9)$$

Inside the atomic spheres APW uses numerical radial functions  $W_{lm}^{n,\alpha,\mathbf{k}}(r)$  computed at predefined linearization energies,<sup>28</sup> which are chosen to match the energies of the corresponding occupied bands. This approach yields basically the exact radial wave functions for all occupied and the first conduction band states. However, it is not a complete basis and not well suited to expand the perturbation of the wave function due to an external magnetic field. We have solved this problem by supplying several additional local orbitals (NMR-LO) with radial wave functions evaluated at higher energies<sup>30</sup> and by augmenting the Green's function in eq 5 by radial functions proportional to  $r(\partial/\partial r)u(r)$  (DUDR).<sup>31</sup> This makes the method basically numerically exact within a given DFT functional.<sup>31</sup>

Specifically we added for all orbital quantum numbers up to  $l = 3$  two DUDR functions with  $l \pm 1$  and eight NMR-LOs at energies such that the corresponding radial wave functions have one additional node inside  $S_{\alpha}$ . Besides that, the NMR calculations within our APW method do not require any other computational parameters considerably different from generally accepted defaults. For the sake of analysis we kept the atomic sphere radii for sulfur atoms in the sulfides series

constant at 2.2 au. The radii for sulfates (1.28 au) had to be chosen much smaller due to the small S–O distances and followed the default WIEN2k setup. Because of these small S–O distances in the sulfates, also the S-2*p* orbitals were treated as band states using an extra LO. The plane wave cut off  $K_{\max}$  for the APW basis set is determined by  $RK_{\max} = 8.0$ , where  $R$  represents the smallest atomic radius in a calculation. The Brillouin zone was sampled with mesh size close to  $0.04 \text{ au}^{-1}$ , with exceptions for  $\text{TiS}_2$  and  $\text{PbS}$  where denser meshes of size  $0.013 \text{ au}^{-1}$  are required. Spin–orbit coupling was considered for  $\text{PbS}$ .

## RESULTS AND DISCUSSION

In this work we analyze the relation between electronic structure and the NMR shielding of  $^{33}\text{S}$  in a series of sulfides

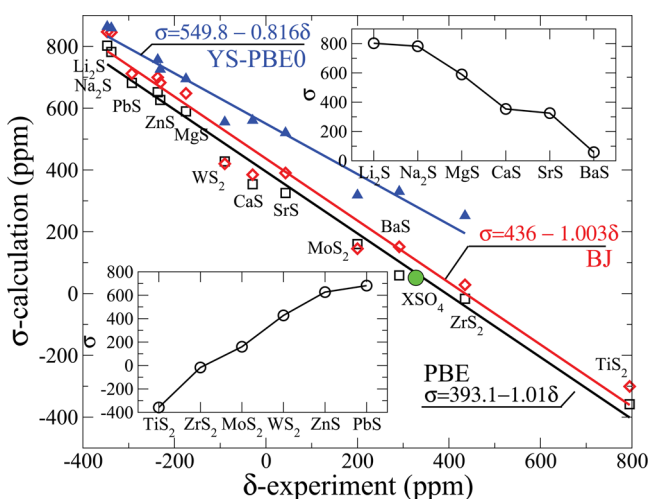


**Figure 1.** Comparison of the experimental  $^{33}\text{S}$  NMR shifts ( $\delta$ ) with the calculated absolute shielding ( $\sigma$ ) for a series of inorganic sulfides computed with the PBE, BJ, and YS-PBE0 functionals, respectively. The insets show the trends for the alkali/alkaline-earth and transition metals sulfides computed with PBE. The larger dot indicates the collective data representing the sulfates. The experimental data have been retrieved from refs 6, 12, and 14.

and sulfates and explain the origin of the huge variation of the NMR shift within the sulfides series. The analysis presented

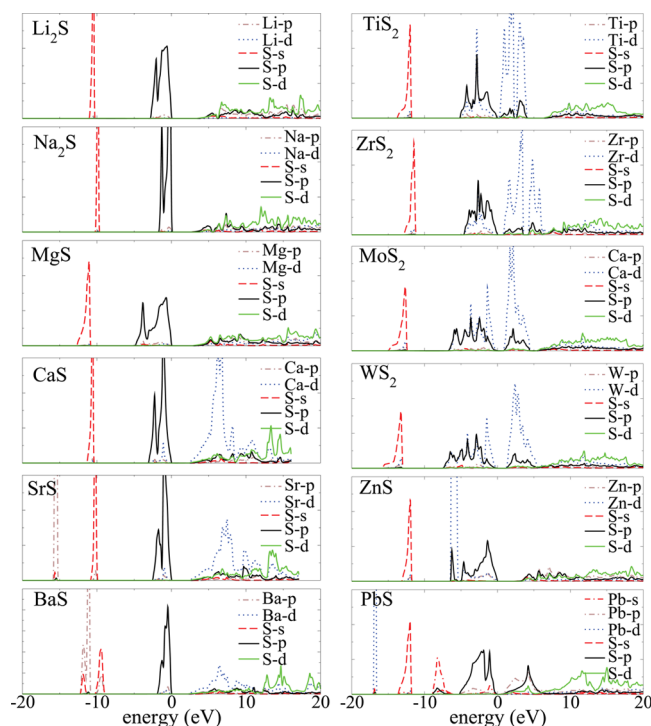


**Figure 2.** Density of states calculated for alkali/alkaline-earth (left) and transition metal sulfides (right).

here follows the strategy applied before to understand the variation of NMR shifts in fluorides.<sup>3</sup> It is based on a decomposition of the total NMR shielding with respect to atomic and orbital character of the occupied and empty states. The analysis is carried out in the following steps: (i) we separate core and valence contributions to the NMR shielding. (ii) The valence part is further split into contributions related to different energy regions as given by individual peaks in the density of states (DOS). (iii) The corresponding main contributions are further decomposed according to the orbital character of the occupied wave functions ( $\Psi_e^{(0)}$ ) and (iv) their perturbations ( $\Psi_e^{(1)}$ ) involved in the expression for the induced current as given in eq 7 ( $\langle \Psi_e^{(0)} | \mathbf{J}^p(\mathbf{r}') | \Psi_e^{(1)} \rangle$ ). The calculation of the perturbation  $\Psi_e^{(1)}$  (given in eq 8) involves empty states  $\Psi_e^{(0)}$  weighted by matrix elements:  $\langle \Psi_e^{(0)} | (\mathbf{r} - \mathbf{r}') \times \mathbf{p} \cdot \mathbf{B} | \Psi_e^{(0)} \rangle$ .

**Table 1.** Structural Parameter of Various Sulfides Together with Computed Absolute  $^{33}\text{S}$  NMR Shielding ( $\sigma$ ) for PBE, BJ, and YS-PBE0 Calculations and Chemical Shifts ( $\delta_{\text{PBE}}$ ) Using the Least Squares Fit Shown in Figure 1) and Comparison with Experimental<sup>6,12–14</sup> Shifts  $\delta_{\text{exp}}$  and Previous PWPP Calculations<sup>11</sup> ( $\sigma_{\text{PWPP}}$ )

	structure	lattice param. (Å)	$\sigma_{\text{BJ}}$	$\sigma_{\text{YS-PBE0}}$	$\sigma_{\text{PBE}}$	$\sigma_{\text{PWPP}}$	$\delta_{\text{PBE}}$	$\delta_{\text{exp}}$
$\text{Li}_2\text{S}$	$Fm\bar{3}m$	5.760	846.88	864.0	802.3	803.6	−411.5	−347
$\text{Na}_2\text{S}$	$Fm\bar{3}m$	6.546	845.37	859.7	781.9	780.5	−391.1	−338
$\text{MgS}$	$Fm\bar{3}m$	5.202	647.90	694.6	589.6	590.7	−198.8	−174.9
$\text{CaS}$	$Fm\bar{3}m$	5.710	384.80	560.4	353.7	354.8	37.1	−29.1
$\text{SrS}$	$Fm\bar{3}m$	6.020	390.13	520.1	325.4	329.0	65.4	42.8
$\text{BaS}$	$Fm\bar{3}m$	6.375	151.37	330.2	58.7	105.0	332.1	291.3
$\text{TiS}_2$	$P\bar{3}m1$	3.4097	5.705	−300.74	−358.4		749.2	795
$\text{ZrS}_2$	$P\bar{3}m1$	3.6623	5.826	28.09	251.8	−17.1	407.9	435
$\text{MoS}_2$	$P63/mmc$	3.1600	12.294	145.22	318.6	160.1	230.7	200
$\text{WS}_2$	$P63/mmc$	3.1530	12.323	420.05	555.0	427.5	−36.7	−90
$\text{ZnS}$	$P63mc$	3.8360	6.277	682.75	725.6	626.5	625.3	−231
$\text{ZnS}$	$F\bar{4}3m$	5.318	699.6	757.0	651.7	660.0	−260.9	−236.5
$\text{PbS}$	$Fm\bar{3}m$	5.932	711.83		788.5		−291.1	−293

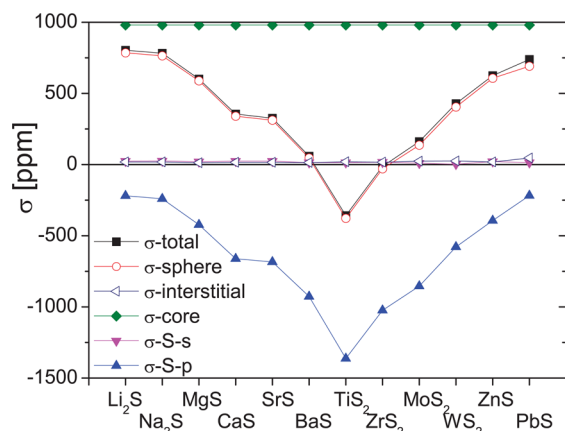


**Figure 3.** Decomposition of the calculated total  $^{33}\text{S}$  NMR shielding ( $\sigma$ -total) into contributions from the S-sphere ( $\sigma$ -sphere) and the rest ( $\sigma$ -interstitial).  $\sigma$ -Sphere is further decomposed into core (S 1s-2p), S 3s-band and S 3p-band contributions.

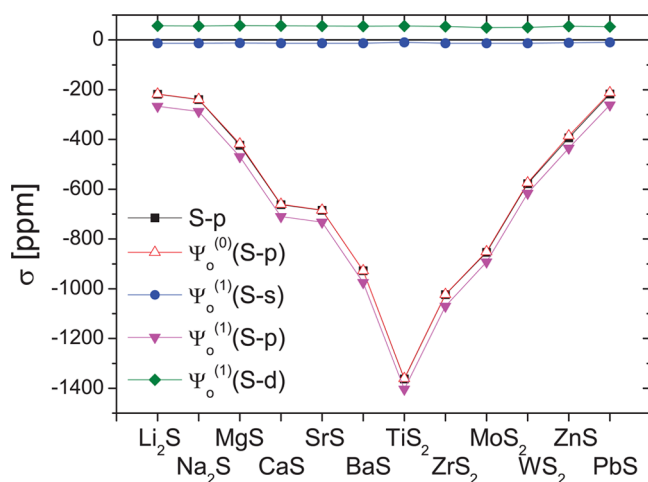


**Figure 4.** Decomposition of the dominant S  $p$ -band contribution (S- $p$ ) with respect to the S- $p$  orbital character of the occupied orbitals ( $\Psi_e^{(0)}(\text{S-}p)$ ) and the orbital character of the corresponding perturbation ( $\Psi_e^{(1)}(\text{S-s}, \text{S-}p, \text{S-d})$ ). The ground state orbitals  $\Psi_e^{(0)}$  and their perturbations  $\Psi_e^{(1)}$  contribute to  $\sigma$  via the induced current given by  $\langle \Psi_e^{(0)} | \mathbf{J}^p(\mathbf{r}') | \Psi_e^{(1)} \rangle$  (see eq 7).

Therefore, in the final step (v), the contributions to  $\tilde{\Psi}_e^{(1)}$  are further decomposed with respect to orbital and atomic components of  $\Psi_e^{(0)}$  involved in these matrix elements. This procedure allows us to identify the atomic and orbital components of the occupied and empty states contributing most to the dominating valence part of the NMR shielding. Subsequently, we can correlate the variation of the NMR shielding across the series of compounds with the differences in the electronic structure of these compounds.

**Sulfides.** Figure 1 compares the calculated NMR shielding ( $\sigma$ ) and measured chemical shifts ( $\delta$ ) for various sulfides. The two insets show the variations of the calculated shielding for alkali/alkaline-earth and transition metal (TM) sulfides separately. The NMR shielding shows a clear monotonic variation within both, the alkali/alkaline-earth and the TM sulfide series. The shielding decreases with the atomic number of the metal atom for the alkali/alkaline-earth series, which is similar to the observed behavior for halides or oxides. However, it increases with the atomic number and the d-band occupancy for TM compounds. Let us mention here that  $\text{TiS}_2$  is metallic

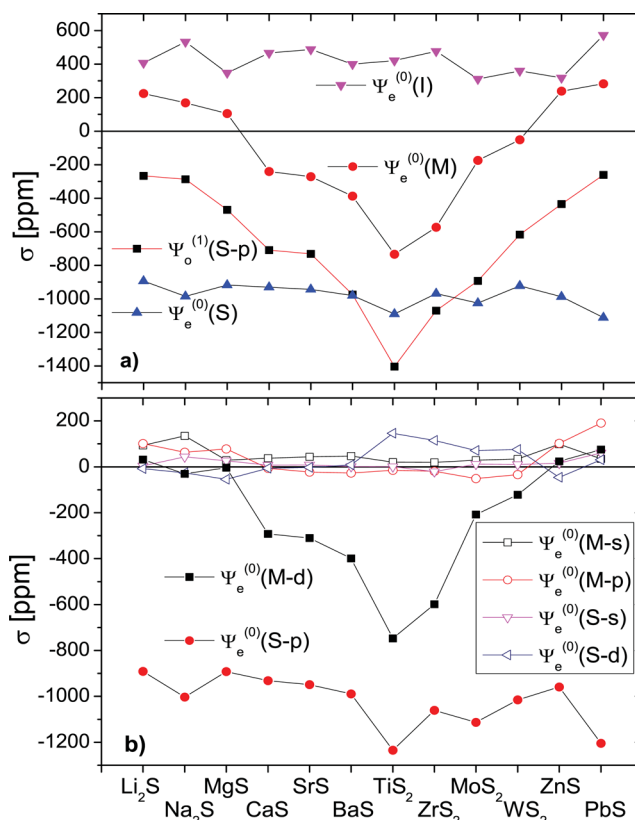


**Figure 5.** Dominant shielding contributions to the first order perturbation with S- $p$  character  $\Psi_e^{(1)}(\text{S-}p)$  with respect to the empty states  $\Psi_e^{(0)}$ , which contribute to the first order perturbation  $\tilde{\Psi}_e^{(1)}$  via the matrix elements  $\langle \Psi_e^{(0)}(\mathbf{r} - \mathbf{r}') \times \mathbf{p} | \mathbf{B} | \Psi_e^{(0)} \rangle$  in eq 8. (a) Decomposition of the integral according to the empty states  $\Psi_e^{(0)}$  in the sulfur (S), metal (M), and interstitial (I) regions; (b) decomposition according to angular momentum of the S and M empty states  $\Psi_e^{(0)}$ .

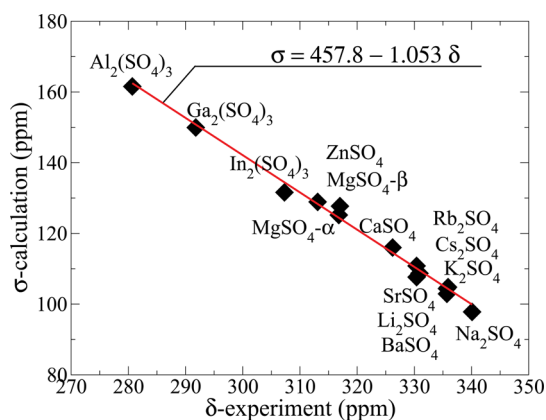


**Figure 6.** Comparison of the experimental  $^{33}\text{S}$  NMR shifts ( $\delta$ ) with calculated absolute shielding ( $\sigma$ ) for series of inorganic sulfates. The experimental data has been taken from ref 14.

and has therefore also a spin-component to the NMR shielding, which is, however, in this material very small (4 ppm) because there are hardly any S  $s$ -states at the valence band maximum. The calculated shielding and measured shifts align well along a straight line over a large range of 1200 ppm and a linear least-squares fit gives  $\sigma = 393.1(12.1) - 1.01(0.04)$  and  $R^2 = 0.984$ . The slope is very close to the required value of  $-1$ , which is at first quite different from the observation in ionic fluorides,

Table 2. Crystal Structure, Cell Parameters (Å), and Optimized S–O Distances (Å) for the Studied Sulfates

	space group	lattice parameters/angles			S–O distance			
Li <sub>2</sub> SO <sub>4</sub> <sup>34</sup>	<i>P21/c</i>	2.9472	8.4740 $\beta = 86.88$	4.9540	1.4939	1.4939	1.4944	1.4992
Na <sub>2</sub> SO <sub>4</sub> <sup>35</sup>	<i>Fddd</i>	5.8582	9.8138	12.2990	1.4997	1.4997	1.4997	1.4997
K <sub>2</sub> SO <sub>4</sub> <sup>36</sup>	<i>Pmcn</i>	5.7704	10.0712	7.4776	1.4928	1.5023	1.5023	1.5055
Rb <sub>2</sub> SO <sub>4</sub> <sup>37</sup>	<i>Pnma</i>	7.8200	5.9790	10.4410	1.4965	1.5039	1.5039	1.5066
Cs <sub>2</sub> SO <sub>4</sub> <sup>37</sup>	<i>Pnma</i>	8.2390	6.2560	10.9370	1.4981	1.5050	1.5050	1.5071
MgSO <sub>4</sub> - $\alpha$ <sup>38</sup>	<i>Cmcm</i>	5.1747	7.8756	6.4952	1.4738	1.4738	1.5007	1.5150
MgSO <sub>4</sub> - $\beta$ <sup>39</sup>	<i>Pnma</i>	8.5787	6.6953	4.7438	1.4738	1.4738	1.5007	1.5150
CaSO <sub>4</sub> <sup>40</sup>	<i>Cmcm</i>	6.9934	6.2417	7.0014	1.4944	1.4944	1.4949	1.4949
SrSO <sub>4</sub> <sup>41</sup>	<i>Pnma</i>	8.3545	5.3458	6.8671	1.4780	1.4780	1.4918	1.5066
BaSO <sub>4</sub> <sup>41</sup>	<i>Pnma</i>	8.8790	5.4540	7.1540	1.4828	1.4944	1.5087	1.5087
ZnSO <sub>4</sub> <sup>42</sup>	<i>Pnma</i>	8.6040	6.7460	4.7740	1.5219	1.4965	1.4801	1.4801
Al <sub>2</sub> (SO <sub>4</sub> ) <sub>3</sub> <sup>43</sup>	$R\bar{3}$	8.0246	8.0246	21.3570	1.4796	1.4891	1.4775	1.4854
Ga <sub>2</sub> (SO <sub>4</sub> ) <sub>3</sub> <sup>44</sup>	$R\bar{3}$	8.0540	8.0540	21.8400	1.4828	1.4933	1.4891	1.4854
In <sub>2</sub> (SO <sub>4</sub> ) <sub>3</sub> <sup>44</sup>	$R\bar{3}$	8.4400	8.4400	23.0930	1.4880	1.4939	1.4912	1.4912
K <sub>2</sub> S <sub>2</sub> O <sub>7</sub> <sup>45</sup>	<i>C2/c</i>	12.3500	7.2700 $\beta = 86.88$	7.3100	1.4579	1.4664	1.4664	1.6727
K <sub>2</sub> S <sub>2</sub> O <sub>8</sub> <sup>46</sup>	<i>P-1</i>	5.1150	5.5050	7.0340	1.4579	1.4626	1.4674	1.6748
		106.32	106.12	90.18				

chlorides, bromides, or oxides, where the slope is usually around  $-1.2$  when using the PBE approximation to DFT.<sup>24</sup> However, a closer look at our results reveals a similar trend and when we restrict the compounds in the fit to alkali and alkaline-earth sulfides, the slope increases to  $-1.18$  and it is quite similar as in the ionic halides and oxide series. It was found previously<sup>24</sup> that in these ionic compounds exchange interactions dominate and the BJ potential, which is an approximation to an optimized exact exchange potential, improves the slope considerably. In the case of the sulfides, however, BJ results are not superior to PBE, and while the slope remains at  $-1.00(0.05)$ , the  $R^2 = 0.969$  value indicates some scatter (MoS<sub>2</sub>, WS<sub>2</sub>) in the results. Obviously, the sulfides are less ionic than halides, and correlations become more important and must be treated on the same footing as exchange. We have also performed rather expensive hybrid-DFT calculations for most sulfides (not for metallic TiS<sub>2</sub> and PbS, where spin-orbit coupling is mandatory). The results are rather disappointing and fairly similar to those for the fluorides.<sup>24</sup> The overall slope ( $-0.82$ ) is far too low with significant scatter ( $R^2 = 0.966$ ). Even considering only the more ionic alkali and alkaline-earth sulfides the slope stays small ( $-0.85$ ), although for these compounds a good  $R^2 = 0.99$  value has been obtained since the most problematic shift for CaS has improved. These rather common observations indicate systematic errors for specific classes of chemical bonding introduced by the various approximations to DFT.

Using the slope and reference value found in the linear fit, as specified in Figure 1, we can also calculate the theoretical chemical shift  $\delta$ . The corresponding numerical data are compared with experiment in Table 1. For the simple sulfides, we can also compare our computed shielding to previous plane-wave pseudopotential (PWPP) calculations<sup>11</sup> using the CASTEP code. We observe in most cases a very good agreement with the published values, except for BaS and PbS, where large differences (50–100 ppm) occur and whose origin is left to speculations. It should be noted that the reference value of 393.1 ppm obtained from the fit compares reasonably with the calculated shift of solid CS<sub>2</sub> (436 ppm). Unfortunately, only the liquid phase of CS<sub>2</sub> is used as a reference in experiment, therefore it is impossible to compute the exact value of the absolute reference shielding.

In the following we discuss the origin of the large variations of the sulfur NMR shielding within series of compounds. For this purpose, we display the atomic and angular momentum resolved partial density of states for the alkali/alkaline-earth and TM compounds in Figure 2. The top of the occupied valence DOS is dominated by states of mainly sulfur-3*p* character (termed S *p*-band) and sulfur-3*s* states (S *s*-band) appear around  $-10$  eV. The S-*p* band is quite narrow for the ionic compounds with small admixture of metal-*d* character. For TM compounds, the metal-*d* character enters the valence band hybridizing with the sulfur-3*p* states. Depending on the number of *d* electrons for a particular TM element their occupation is smaller (TiS<sub>2</sub>, which is still metallic in PBE, and ZrS<sub>2</sub>) or larger (MoS<sub>2</sub>, WS<sub>2</sub>) until the *d* shell becomes fully occupied for ZnS (still overlapping with S-*p*) and PbS (localized Pb-5*d* peak around  $-15$  eV). For all compounds except Li<sub>2</sub>S there is also a low-lying metal-*p* band, which approaches the S *s*-band in SrS and BaS. The conduction band is dominated by metal-*d* character (except for Li<sub>2</sub>S, Na<sub>2</sub>S, MgS, ZnS, and PbS), followed by sulfur-*p* and sulfur-*d* character. As we will show below, the changes of metal-*d* character is the dominating effect determining the magnetic shielding. For Li<sub>2</sub>S, Na<sub>2</sub>S, and MgS there is no metal-*d* character in the vicinity of the band gap, while for the other metal atoms it is gradually coming down in energy and eventually relocated between the conduction and the valence bands until it is well below the S-*p* valence band in PbS.

In the first step of our analysis we identify the leading contributions to the total shielding within the series of our compounds. Figure 3 shows that the total shielding is a fairly local quantity and comes predominantly from an integral over the current within the sulfur atomic sphere ( $\sigma$ -sphere), while the contributions from the interstitial and the metal-spheres ( $\sigma$ -interstitial) are small. We can thus restrict our analysis to the contributions within the S-sphere. The largest contribution (979.9 ppm) comes usually from the S-core electrons (1*s*, 2*s*, 2*p*), but this contribution is absolutely constant within the series. Clearly, the main contribution explaining the observed trend comes from the S *p*-band, while the sulfur *s*-band contribution is below 25 ppm for all compounds (and also entirely of S-3*p* character). The contributions of other bands (not shown in Figure 3) are always below 10 ppm, except for

Table 3. Comparison of Calculated and Experimental  $^{33}\text{S}$  NMR Parameters<sup>a</sup>

		$\sigma_{\text{iso}}$	$\Delta\sigma_{\text{aniso}}$	$\eta_{\text{CSA}}$	$\delta$	$C_Q$	$\eta_Q$
$\text{Li}_2\text{SO}_4$	WIEN2k	108.7	16.8	0.62	331.7	1.028	0.52
	experiment		$19.0 \pm 2.0$	$0.4 \pm 0.1$	$330.9 \pm 0.5$	$0.877 \pm 0.05$	$0.91 \pm 0.05$
	CASTEP	105.8	16.4	0.79	328.3	1.023	0.66
$\text{Na}_2\text{SO}_4$	WIEN2k	97.8	-4.08	0.77	342.1	-0.531	0.54
	experiment		$-15.6 \pm 2.0$	$0.1 \pm 0.1$	$340.1 \pm 1.0$	$0.655 \pm 0.05$	$0.0 \pm 0.1$
	CASTEP	93.5	2.9	0.79	340.1	-0.697	0.26
$\text{K}_2\text{SO}_4$	WIEN2k	104.4	20.11	0.37	335.8	0.739	0.47
	experiment		-17.5	$0.3 \pm 0.1$	$335.7 \pm 0.5$	$0.959 \pm 0.03$	$0.42 \pm 0.05$
	CASTEP	92.4	17.8	0.45	341.7	0.788	0.53
$\text{Rb}_2\text{SO}_4$	WIEN2k	102.9	18.48	0.13	337.2	0.680	0.46
	experiment		$-17.0 \pm 2.0$	$0.4 \pm 0.1$	$335.7 \pm 0.6$	$0.860 \pm 0.05$	$0.42 \pm 0.1$
	CASTEP	93.0	21.5	0.25	341.1	0.865	0.44
$\text{Cs}_2\text{SO}_4$	WIEN2k	104.8	20.76	0.16	335.4	0.643	0.48
	experiment		$-14 \pm 2.0$	$0.4 \pm 0.2$	$335.9 \pm 1.0$	$0.813 \pm 0.05$	$0.4 \pm 0.1$
	CASTEP	95.6	21.0	0.17	338.5	0.718	0.46
$\text{MgSO}_4\text{-}\alpha$	WIEN2k	128.9	54.53	0.97	312.5	-1.371	0.82
	experiment		$-51.5 \pm 3.0$	$0.9 \pm 0.1$	$313.1 \pm 2.0$	$2.14 \pm 0.05$	$0.91 \pm 0.5$
	CASTEP	118.8	49.9	0.97	315.3	-1.846	0.88
$\text{MgSO}_4\text{-}\beta$	WIEN2k	125.2	-43.64	0.22	316.0	-1.636	0.30
	experiment		$-37.6 \pm 3.0$	$0.1 \pm 0.1$	$316.8 \pm 2.0$	$2.0 \pm 0.05$	$0.11 \pm 0.1$
	CASTEP	115.4	-42.4	0.18	318.7	-1.886	0.25
$\text{CaSO}_4$	WIEN2k	116.0	-23.09	0.88	324.8	1.031	0.47
	experiment		$18.3 \pm 2.0$	$0.9 \pm 0.2$	$326.2 \pm 0.5$	$0.86 \pm 0.05$	$0.48 \pm 0.1$
	CASTEP	110.4	20.7	0.81	323.7	0.925	0.03
$\text{SrSO}_4$	WIEN2k	107.6	35.06	0.87	332.8	0.897	0.93
	experiment		$30.0 \pm 3.0$	$0.9 \pm 0.3$	$330.4 \pm 1.0$	$1.31 \pm 0.05$	$0.84 \pm 0.1$
	CASTEP	98.9	35.8	0.79	335.2	1.121	0.95
$\text{BaSO}_4$	WIEN2k	110.8	44.59	0.75	329.7	1.261	0.85
	experiment		$28.0 \pm 4.0$	$0.8 \pm 0.3$	$330.4 \pm 2.0$	$1.76 \pm 0.05$	$0.68 \pm 0.05$
	CASTEP	99.1	44.7	0.75	335.0	1.559	0.79
$\text{ZnSO}_4$	WIEN2k	127.7	-47.65	0.24	313.6	-1.743	0.86
	experiment		$-56.3 \pm 4.0$	$0.2 \pm 0.2$	$317.0 \pm 0.5$	$2.04 \pm 0.05$	$0.54 \pm 0.05$
	CASTEP	117.9	-47.5	0.22	316.2	-1.917	0.91
$\text{Al}_2(\text{SO}_4)_3$	WIEN2k	161.6	26.06	0.30	281.3	-2.400	0.56
	experiment		$31.0 \pm 5.0$	$0.4 \pm 0.3$	$280.7 \pm 2.0$	$2.32 \pm 0.05$	$0.55 \pm 0.05$
	CASTEP	156.4	27.4	0.38	277.7	-2.680	0.53
$\text{Ga}_2(\text{SO}_4)_3$	WIEN2k	149.9	29.81	0.48	292.5	-1.820	0.64
	experiment		$24.0 \pm 4.0$	$0.4 \pm 0.2$	$291.8 \pm 1.0$	$1.87 \pm 0.05$	$0.68 \pm 0.1$
	CASTEP	143.5	30.2	0.35	290.6	-1.928	0.64
$\text{In}_2(\text{SO}_4)_3$	WIEN2k	131.6	23.56	0.83	309.9	-1.172	0.93
	experiment		$22.2 \pm 5.0$	$0.7 \pm 0.2$	$307.3 \pm 0.5$	$1.25 \pm 0.05$	$0.88 \pm 0.1$
	CASTEP	126.6	24.0	0.66	307.6	-1.32	0.90
$\text{K}_2\text{S}_2\text{O}_7$	WIEN2k	127.9	-199.37	0.22	313.4	-11.986	0.10
	experiment				320	16.2	0.1
	CASTEP	141.8	208.2	0.09	293.1	15.16	0.39
$\text{K}_2\text{S}_2\text{O}_8$	WIEN2k	116.4	-188.56	0.17	324.4	-11.569	0.06
	experiment				330	15.9	0.1
	CASTEP	139.1	190.8	0.11	280	14.96	0.07

<sup>a</sup>The experimental and CASTEP calculated values are taken from ref 11 for  $\text{K}_2\text{S}_2\text{O}_7$  and  $\text{K}_2\text{S}_2\text{O}_8$  and from ref 14 for all others.

the high-lying Ba  $5p$ -band in BaS (see Figure 2) with 19.9 ppm and the fully occupied Pb  $5d$ -band in PbS with -85.9 ppm, where these bands contribute 30 (10)% to the total shielding.

The next step of our analysis is summarized in Figure 4, where the dominant sulfur  $p$ -band contribution is decomposed with respect to the orbital character of the unperturbed occupied ground-state  $\Psi_0^{(0)}$  and the corresponding perturbed states  $\tilde{\Psi}_0^{(1)}$ .  $\Psi_0^{(0)}$  and  $\tilde{\Psi}_0^{(1)}$  contribute to the induced current by  $\langle \Psi_0^{(0)} | \mathbf{J}^p(\mathbf{r}') | \tilde{\Psi}_0^{(1)} \rangle$ , as given in eq 7. As expected, the  $S$ - $p$  ( $l = 1$ ) component of  $\Psi_0^{(0)}$  delivers nearly the whole value of the

shielding. Also, for the first order perturbation  $\tilde{\Psi}_0^{(1)}$  the  $S$ - $p$  contribution dominates and dictates the trend, while the  $S$ - $s$  and  $S$ - $d$  components are fairly small and constant within the series. In order to understand the origin of the shielding variations, we may focus only on the  $l_0 = 1$  and  $l_{\text{top}} = 1$  components of  $\Psi_0^{(0)}$  and  $\tilde{\Psi}_0^{(1)}$ , respectively, and the resulting contribution to the induced current.

Figure 5 shows the decomposition of the  $l_0 = 1$ ,  $l_{\text{top}} = 1$  component of the valence  $\sigma$  ( $\tilde{\Psi}_0^{(1)}(S$ - $p)$ ) with respect to the atomic and orbital character  $l_e$  of the empty states  $\Psi_e^{(0)}$

Table 4. Decomposition of the Total Magnetic Shielding into Core (979.9 ppm in all cases) and Valence Contributions in Selected Sulfates<sup>a</sup>

	total	valence	S-sph.	$S_{l_{\text{top}}=1}^{l_e=1}$	inter.	metal	S	O
Na <sub>2</sub> SO <sub>4</sub>	97.8	-882.2	-893.9	-868.0	-451.1	-5.2	-314.1	-97.6
						$l_e = 0$ : -2.8	$l_e = 0$ : 0.0	$l_e = 0$ : 89.1
						$l_e = 1$ : -1.8	$l_e = 1$ : -309.2	$l_e = 1$ : -109.6
						$l_e = 2$ : -0.1	$l_e = 2$ : -5.0	$l_e = 2$ : -73.3
MgSO <sub>4</sub>	125.2	-854.7	-863.7	-836.2	-437.9	-3.7	-306.0	-85.7
						$l_e = 0$ : -1.5	$l_e = 0$ : 0.0	$l_e = 0$ : 96.0
						$l_e = 1$ : -1.6	$l_e = 1$ : -301.3	$l_e = 1$ : -107.2
						$l_e = 2$ : -0.0	$l_e = 2$ : -4.6	$l_e = 2$ : -71.2
BaSO <sub>4</sub>	110.8	-869.1	-879.5	-852.1	-458.7	5.9	-308.0	-91.206
						$l_e = 0$ : -1.9	$l_e = 0$ : 0.1	$l_e = 0$ : 89.8
						$l_e = 1$ : 3.9	$l_e = 1$ : -303.2	$l_e = 1$ : -107.4
						$l_e = 2$ : 3.8	$l_e = 2$ : -4.9	$l_e = 2$ : -70.1
MgSO <sub>4</sub> with BaSO <sub>4</sub> structure	95.9	-884.0	-893.4	-869.4	-468.9	-0.7	-309.5	-90.3
						$l_e = 0$ : -0.3	$l_e = 0$ : 0.1	$l_e = 0$ : 88.4
						$l_e = 1$ : -0.3	$l_e = 1$ : -304.7	$l_e = 1$ : -105.4
						$l_e = 2$ : 0.0	$l_e = 2$ : -4.8	$l_e = 2$ : -69.8
BaSO <sub>4</sub> with MgSO <sub>4</sub> structure	206.0	-773.9	-782.5	-754.8	-386.7	55.5	-314.6	-109.1
						$l_e = 0$ : -15.7	$l_e = 0$ : -0.4	$l_e = 0$ : 86.3
						$l_e = 1$ : 21.5	$l_e = 1$ : -311.1	$l_e = 1$ : -112.3
						$l_e = 2$ : 49.6	$l_e = 2$ : -3.0	$l_e = 2$ : -79.5

<sup>a</sup>The valence contribution from inside the S-sphere comes primarily from  $S(l_o = 1, l_{\text{top}} = 1)$  components. The latter is further decomposed with respect to its atomic and orbital character  $l_e$  of the empty states  $\Psi_e^{(0)}$  contributing to the first order perturbation  $\tilde{\Psi}_o^{(1)}$  via the matrix elements:  $\langle \Psi_e^{(0)} | (\mathbf{r} - \mathbf{r}') \times \mathbf{p} \cdot \mathbf{B} | \Psi_o^{(0)} \rangle$  in eq 8 (all values in ppm).

appearing in the expression for the first order perturbation  $\tilde{\Psi}_o^{(1)}$  (see eq 8). Contrary to the decomposition shown in Figure 4, where only the sulfur atomic sphere needs to be considered, here the integral  $\langle \Psi_e^{(0)} | (\mathbf{r} - \mathbf{r}') \times \mathbf{p} \cdot \mathbf{B} | \Psi_o^{(0)} \rangle$  over the whole unit cell has to be taken into account. In Figure 5a we decompose this integral according to the APW approach into three regions, namely, sulfur (S) and metal (M) spheres and an interstitial (I) part. Because the empty conduction band states are not well localized within the atomic sphere a large fraction of the integral comes from the interstitial and cannot be uniquely assigned to a specific atomic and orbital character of the corresponding wave functions. Although the resulting NMR shielding related to this part of  $\langle \Psi_e^{(0)} | (\mathbf{r} - \mathbf{r}') \times \mathbf{p} \cdot \mathbf{B} | \Psi_o^{(0)} \rangle$  is substantial (about 400 ppm), it is relatively constant and the variation barely exceeds 200 ppm (Figure 5a). The component related to the sulfur sphere ( $\Psi_e^{(0)}(S)$ ) is even larger (around -1000 ppm), but its variation within the series is again only 200 ppm and cannot explain the observed trends. Surprisingly the leading term which determines the observed trends of the total shielding comes from the integral involving the metal sphere ( $\Psi_e^{(0)}(M)$ ) in Figure 5a).

In order to better understand this fact, we decompose in Figure 5b the contributions of the metal and sulfur sphere according to their  $l_e$  character. The operator in the matrix elements  $\langle \Psi_e^{(0)} | (\mathbf{r} - \mathbf{r}') \times \mathbf{p} \cdot \mathbf{B} | \Psi_o^{(0)} \rangle$  is a product of position and momentum operators, therefore the selection rules for coupling  $\Psi_e^{(0)}$  and  $\Psi_o^{(0)}$  follows  $\Delta l = 0, \pm 1$ . As shown before, the valence states  $\Psi_o^{(0)}$  contributing to the NMR shift are mainly of sulfur  $l_o = 1$  character and they can couple to  $l_e = 0, 1, 2$  character. Let us first summarize that the contributions of the sulfur  $s, p,$  and  $d,$  as well as of the metal  $s$  and  $p$  character of the unoccupied states are small and vary typically by about 100–200 ppm within the series (see Figure 5b). For both valence and conduction band states, the  $l_o = 1$  and  $l_e = 1$  sulfur components are large, but do not vary substantially within the sulfide series,

leading to a large but fairly constant component to the shielding (see  $\Psi_e^{(0)}(S-p)$  in Figure 5b). In the end it turns out that the contribution of the  $d$ -component of the metal wave functions are most important. Specifically,  $\Psi_e^{(0)}(M-d)$  in Figure 5b is the metal  $l_e = 2$  component of the conduction band states  $\langle \Psi_e^{(0)} |$  and the leading term which determines the observed trends of the NMR shielding in the sulfides. This metal- $d$  contribution of the conduction band states dictates also the different trends seen in the alkali/alkaline-earth and the transition metal compounds. The trends in the alkali/alkaline-earth sulfides are similar to those in the corresponding fluorides,<sup>3</sup> and the coupling of the sulfur (fluorine) valence states to the metal  $l_e = 2$  character of the conduction states results in an increase of the absolute value of this contribution to the shielding when going down the periodic table, because the metal  $d$ -states come down in energy and closer to the conduction band minimum. For the TM elements the contribution to the shielding arranges according to the filling of the  $d$ -band. The largest absolute value (most negative value) is observed for TiS<sub>2</sub>, where there is a completely empty  $l_e = 2$  conduction band, which is reduced when more and more  $d$  electrons become occupied across the TM series until the  $d$ -bands are filled for ZnS and PbS, so that there is hardly any  $d$ -character at the bottom of the conduction band. Therefore, the metal- $d$  band contribution, and thus the total NMR shielding, is quite similar in otherwise very different compounds like ZnS, PbS and Na<sub>2</sub>S, MgS.

**Sulfates.** The <sup>33</sup>S NMR shielding in sulfates is determined primarily by the sulfur–oxygen interaction. The absolute shielding varies only by about 60 ppm among the studied compounds (see Figure 6 and Table 3) and is roughly correlated with the deformations of the oxygen tetrahedra. We stress that an optimization of the internal atomic coordinates was absolutely mandatory to get good correlation between experimental and theoretical NMR data (we still used

experimental lattice parameters). The structural details, lattice parameters and optimized S–O distances are given in Table 2. A linear fit of the computed absolute shielding versus the measured shifts (using all data shown in Figure 6) has a slope of  $-1.05(0.03)$ , which is very close to that in the sulfides, but the reference constant from the least-square fit ( $457.8(9.0)$  ppm) is considerably larger than for the sulfides ( $393.1$  ppm). On the other hand, this value is closer to the computed shielding of  $435.3$  ppm for the reference compound  $\text{CS}_2$  providing better internal consistency than for the sulfides, where the fitted reference value is about  $42$  ppm different from the shielding in  $\text{CS}_2$ . The discrepancy may result from the fact that sulfur in  $\text{CS}_2$  is also covalently bonded and chemically closer to sulfates than to ionic sulfides. In general there is excellent agreement between our results and recent experimental values<sup>14</sup> (less than  $3$  ppm, see Table 3), while older experiments<sup>4,9,11</sup> would sometimes show significantly larger differences. For  $\text{K}_2\text{S}_2\text{O}_7$ ,  $\text{K}_2\text{S}_2\text{O}_8$  the experimental results<sup>11</sup> carry larger uncertainties, probably due to large  $C_Q$  values, causing some deviations between theory and experiment. Our WIEN2k results are also close to recently published theoretical values<sup>14</sup> of  $\sigma_{\text{iso}}$  computed with CASTEP (as these authors have made calculations for various structures, we have taken their values after geometry optimization, but still lattice parameters may differ in a few cases), and the discrepancy does not exceed  $10$  ppm in most cases and is fairly systematic, as all CASTEP values are smaller than ours. Again, there are larger discrepancies for  $\text{K}_2\text{S}_2\text{O}_7$ ,  $\text{K}_2\text{S}_2\text{O}_8$ , probably because the structures have not been geometry optimized in these two older calculations.<sup>11</sup> The quite good agreement between WIEN2k and CASTEP also holds for  $\Delta\sigma_{\text{aniso}}$  and the asymmetry parameter  $\eta_{\text{CSA}}$  (except for  $\text{CaSO}_4$ , where the values have even opposite sign), although these values are even more sensitive to small structural differences. For completeness we have also included in Table 3 the results of the quadrupolar coupling constant  $C_Q$  and the asymmetry parameter  $\eta_Q$ , which describes the electric field gradient tensor. Again, the agreement between present and previous calculations<sup>14</sup> is pretty good for these sensitive quantities, the largest difference occurs for  $C_Q$  in  $\alpha\text{-MgSO}_4$  and for  $\eta_Q$  in  $\text{CaSO}_4$ .

The considerable difference of sphere sizes of the sulfur atom in the sulfates ( $1.28$  au) and sulfides ( $2.2$  au) and the very different nature of the chemical bonding makes it difficult to compare these two classes of compounds directly. Although the direct bonding neighbors of S do not change in the series of sulfates ( $\text{SO}_4$  tetrahedra), it is certainly informative to decompose the shielding for a few sulfates in the same way as it was done for the sulfides. We have chosen the sulfates with the small ( $\text{Na}_2\text{SO}_4$ ) and with the large ( $\text{MgSO}_4$ ) shielding, but also  $\text{BaSO}_4$ , which has the same structure (space group) as  $\text{MgSO}_4$ . In order to separate the influence of geometry (bond distances and angles) and the metal atom, we also performed fictitious calculations for  $\text{BaSO}_4$  with the structural parameters of  $\text{MgSO}_4$  and vice versa. Table 4 summarizes the analysis for these sulfates. As mentioned before, the total value of the shielding varies only by about  $30$  ppm from  $\text{Na}_2\text{SO}_4$  to  $\text{MgSO}_4$  ( $97.9$  and  $128.4$  ppm). The core contribution is the same as in the sulfides and the valence shielding comes primarily from the current within the sulfur sphere of radius  $1.28$  au. The orbital decomposition of stage two shows the same trend as in the sulfides and almost the whole shielding originates from the  $S\text{-}p$  states, both for the ground state as well as for the perturbation due to the magnetic field (labeled  $S(l_o = 1, l_{\text{fp}} = 1)$  in Table 4).

In the calculation of the first order perturbation  $\tilde{\Psi}_o^{(1)}$ , the empty states  $\Psi_e^{(0)}$  contribute via the matrix elements given in eq 8 and the corresponding integrals are divided into contributions from the interstitial and the different atomic spheres with selected angular momentum character. As can be seen from Table 4, the difference between  $\text{Na}_2\text{SO}_4$  and  $\text{MgSO}_4$  comes from the interstitial, the S and the O spheres in about the same amount and cannot be assigned to a single specific orbital character. As expected, the metal contribution is in both cases very small because the metal  $d$ -states are at very high energies, a result in agreement with  $\text{Na}_2\text{S}$  and  $\text{MgS}$ . The different shielding properties have therefore primarily structural origin.

When going from  $\text{MgSO}_4$  to  $\text{BaSO}_4$ , the shielding is reduced by  $18$  ppm, which is more than an order of magnitude smaller reduction than in  $\text{MgS}$ - $\text{BaS}$ . This reduction, however, comes mainly from oxygen and interstitial contributions, while in fact the large negative contribution due to  $\Psi_e^{(0)}(\text{Ba})$  in  $\text{BaS}$  ( $-400$  ppm, see Figure 5b) is now even slightly positive because the direct phase relationship between  $\text{Ba-}d$  and  $\text{S-}p$  states is not present in the sulfates. The direct influence of the metal atom on the shielding can be demonstrated by calculations for  $\text{BaSO}_4$  using the  $\text{MgSO}_4$  structure, and vice versa,  $\text{MgSO}_4$  with  $\text{BaSO}_4$  structure. Changing Ba for Mg in the  $\text{MgSO}_4$  structure almost doubles the shielding to  $206$  ppm and as can be seen from Table 4, the main difference comes from the metal atom contribution (and the interstitial) when calculating the perturbation, since the empty  $\text{Ba-}d$  states are much closer to the valence bands and can effectively contribute to the polarization of the ground state due to the magnetic field but, as mentioned above, with a different sign than in  $\text{BaS}$ . In the real  $\text{BaSO}_4$  structure, however, the distance between Ba and O is much larger resulting in a considerably smaller direct metal contribution. For  $\text{MgSO}_4$  with  $\text{BaSO}_4$  structure the shielding is reduced to  $95.9$  ppm, mainly due to the reduction of the metal (and interstitial) contribution, because the (small) positive Ba contribution is lacking when Ba is replaced by Mg.

## CONCLUSIONS

In this work we have used density functional theory and a first order perturbation approach to calculate the  $^{33}\text{S}$  nuclear magnetic shielding in various sulfides and sulfates. We could successfully reproduce the experimentally observed large variations of  $\sigma$  in the range of  $1200$  ppm within the investigated compounds. The overall slope of the correlation between theory and experiment is very close to the required value of  $-1$ , while when we restrict the comparison to the ionic alkali/alkaline-earth sulfides, a larger slope would arise as found previously also in ionic halides. The BJ functional also yields a slope close to  $-1$ , while when the hybrid-DFT functional YS-PBE0 is used, a significantly smaller slope than  $-1$  results and overall the PBE functional yields the best description. In the sulfides, the relevant induced current and the corresponding variations of the magnetic shielding are generated nearly solely by the sulfur- $p$  ( $l = 1$ ) component of the ground state valence wave functions and their perturbations due to the magnetic field. Within our approach, the perturbation of the valence wave function is determined by a coupling between valence and conduction band states. An analysis indicates that the change of the magnetic shielding within the series originates from the change of the coupling to the conduction band metal- $d$  character. The shielding in the sulfides scales well with the energetic position and the amount of metal  $l_e = 2$  character in the conduction band. Thus, for metals like Li, Na (Mg), or Pb

(Zn), the valence shielding is small, and the large total shielding is close to the diamagnetic core contribution. On the other hand, for heavier alkali/alkaline-earth and early TM sulfides, the shielding decreases (in BaS it is almost zero and in TiS<sub>2</sub> it even changes sign). However, when the occupancy of the *d* shell increases within the series of TM compounds, the valence contribution reduces again, and in ZnS and PbS, we are back to a shielding, as in MgS. In the case of sulfates, the variation of the shielding is very small as compared to the sulfides. Still, our calculations capture correctly the variations and are able to correctly distinguish the particular sulfate compounds.

## AUTHOR INFORMATION

### Corresponding Author

\*E-mail: rolask@ihpc.a-star.edu.sg.

### Notes

The authors declare no competing financial interest.

## ACKNOWLEDGMENTS

We would like to acknowledge support by the Austrian Science Foundation (F.W.F.) in Project SFB-F41 (ViCoM). This work was supported by the A\*STAR Computational Resource Centre through the use of its high performance computing facilities.

## REFERENCES

- (1) Kaupp, M.; Bühl, M.; Malkin, V. G., Eds. *Calculation of NMR and EPR Parameters. Theory and Applications*; Wiley: New York, 2004.
- (2) Grant, C. M.; Harris, R. K., Eds. *Encyclopedia of NMR*; Wiley: New York, 1996.
- (3) Laskowski, R.; Blaha, P. Origin of NMR Shielding in Fluorides. *Phys. Rev. B* **2012**, *85*, 245117–245123.
- (4) Eckert, H.; Yesinowski, J. P. Sulfur-33 NMR at Natural Abundance in Solids. *J. Am. Chem. Soc.* **1986**, *108*, 2140–2146.
- (5) Bastow, T. J.; Stuart, S. N. NMR Study of the Zinc Chalcogenides (ZnX, X = O, S, Se, Te). *Phys. Stat. Solidi B* **1988**, *145*, 719–728.
- (6) Daunch, W. A.; Rinaldi, P. L. Natural-Abundance Solid-State <sup>33</sup>S NMR with High-Speed Magic-Angle Spinning. *J. Magn. Reson., A* **1996**, *123*, 219–221.
- (7) Jakobsen, H. J.; Hove, A. R.; Bildsøe, H.; Skibsted, J. Satellite Transitions in Natural Abundance Solid-State <sup>33</sup>S MAS NMR of Alums-Sign Change with Zero-Crossing of CQ in a Variable Temperature Study. *J. Magn. Reson.* **2006**, *180*, 170–177.
- (8) d'Espinose de Lacaillerie, J.-B.; Barberon, F.; Bresson, B.; Fonollosa, P.; Zanni, H.; Fedorov, V. E.; Naumov, N. G.; Gan, Z. Applicability of Natural Abundance <sup>33</sup>S Solid-State NMR to Cement Chemistry. *Cem. Concr. Res.* **2006**, *36*, 1781–1783.
- (9) Wagler, T. A.; Daunch, W. A.; Panzner, M.; Youngs, W. J.; Rinaldi, P. L. Solid-State <sup>33</sup>S MAS NMR of Inorganic Sulfates. *J. Magn. Reson.* **2004**, *170*, 336–344.
- (10) Couch, S.; Howes, A.; Kohn, S.; Smith, M. <sup>33</sup>S Solid State NMR of Sulphur Speciation in Silicate Glasses. *Solid State Nucl. Magn. Reson.* **2004**, *26*, 203–208.
- (11) Moudrakovski, I.; Lang, S.; Patchkovskii, S.; Ripmeester, J. High Field <sup>33</sup>S Solid State NMR and First-Principles Calculations in Potassium Sulfates. *J. Phys. Chem. A* **2010**, *114*, 309–316.
- (12) Wagler, T. A.; Daunch, W. A.; Rinaldi, P. L.; Palmer, A. R. Solid State <sup>33</sup>S NMR of Inorganic Sulfides. *J. Magn. Reson.* **2003**, *161*, 191–197.
- (13) Sutrisno, A.; Terskikh, V. V.; Huang, Y. A Natural Abundance <sup>33</sup>S Solid-State NMR Study of Layered Transition Metaldisulfides at Ultrahigh Magnetic Field. *Chem. Commun.* **2009**, 186–188.
- (14) Pallister, P. J.; Moudrakovski, I. L.; Enright, G. D.; Ripmeester, J. A. Structural Assessment of Anhydrous Sulfates with High Field <sup>33</sup>S Solid State NMR and First Principles Calculations. *CrystEngComm* **2013**, *15*, 8808–8822.
- (15) Helgaker, T.; Jaszunski, M.; Ruud, K. Ab Initio Methods for the Calculation of NMR Shielding and Indirect Spin-Spin Coupling Constants. *Chem. Rev.* **1999**, *99*, 293–352.
- (16) Mauri, F.; Pfrommer, B. G.; Louie, S. G. Ab Initio Theory of NMR Chemical Shifts in Solids and Liquids. *Phys. Rev. Lett.* **1996**, *77*, 5300–5303.
- (17) Sebastiani, D.; Parrinello, M. A New ab-Initio Approach for NMR Chemical Shifts in Periodic Systems. *J. Phys. Chem. A* **2001**, *105*, 1951–1958.
- (18) Pickard, C. J.; Mauri, F. All-Electron Magnetic Response with Pseudopotentials: NMR Chemical Shifts. *Phys. Rev. B* **2001**, *63*, 245101–245114.
- (19) Yates, J. R.; Pickard, C. J.; Mauri, F. Calculation of NMR Chemical Shifts for Extended Systems Using Ultrasoft Pseudopotentials. *Phys. Rev. B* **2007**, *76*, 024401–024412.
- (20) Thonhauser, T.; Ceresoli, D.; Mostofi, A. A.; Marzari, N.; Resta, R.; Vanderbilt, D. A Converse Approach to the Calculation of NMR Shielding Tensors. *J. Chem. Phys.* **2009**, *131*, 101101–101105.
- (21) Skachkov, D.; Krykunov, M.; Ziegler, T. An Improved Scheme for the Calculation of NMR Chemical Shifts in Periodic Systems Based on Gauge Including Atomic Orbitals and Density Functional Theory. *Can. J. Chem.* **2011**, *89*, 1150–1161.
- (22) Hohenberg, P.; Kohn, W. Inhomogeneous Electron Gas. *Phys. Rev.* **1964**, *136*, B864–B871.
- (23) Kohn, W.; Sham, L. J. Self-Consistent Equations Including Exchange and Correlation Effects. *Phys. Rev. A* **1965**, *140*, 1133–1138.
- (24) Laskowski, R.; Blaha, P.; Tran, F. Assessment of DFT Functionals with NMR Chemical Shifts. *Phys. Rev. B* **2013**, *87*, 195130–195138.
- (25) Perdew, J.; Burke, K.; Ernzerhof, M. Generalized Gradient Approximation Made Simple. *Phys. Rev. Lett.* **1996**, *77*, 3865–3868.
- (26) Becke, A. D.; Johnson, E. R. A Simple Effective Potential for Exchange. *J. Chem. Phys.* **2006**, *124*, 221101–221105.
- (27) Tran, F.; Blaha, P. Implementation of Screened Hybrid Functionals Based on the Yukawa Potential within the LAPW Basis Set. *Phys. Rev. B* **2011**, *83*, 235118.
- (28) Singh, D. J.; Nordström, L. *Planewaves, Pseudopotentials and the LAPW Method*, 2<sup>nd</sup> ed.; Springer: New York, 2006.
- (29) Blaha, P.; Schwarz, K.; Madsen, G. K. H.; Kvasnicka, D.; Luitz, J. *WIEN2k, An Augmented Plane Wave Plus Local Orbitals Program for Calculating Crystal Properties*; Karl-Heinz Schwarz, Techn. Universit.: Wien, 2001.
- (30) Laskowski, R.; Blaha, P. Calculations of NMR Chemical Shifts with APW-Based Methods. *Phys. Rev. B* **2012**, *85*, 035132–035144.
- (31) Laskowski, R.; Blaha, P. Calculating NMR Chemical Shifts Using the Augmented Plane-Wave Method. *Phys. Rev. B* **2014**, *89*, 014402–014409.
- (32) Gregor, T.; Mauri, F.; Car, R. A Comparison of Methods for the Calculation of NMR Chemical Shifts. *J. Chem. Phys.* **1999**, *111*, 1815–1822.
- (33) Powell, B. M.; Dolling, G.; Torrie, B. H. Structure of Solid Carbon Disulphide Between 5 and 150 K. *Acta Crystallogr., Sect. B* **1982**, *38*, 28–32.
- (34) Nord, A. G. Crystal Structure of  $\beta$ -Li<sub>2</sub>SO<sub>4</sub>. *Acta Crystallogr., Sect. B* **1976**, *32*, 982–983.
- (35) Rasmussen, S. E.; Jørgensen, J.-E.; Lundtoft, B. Structures and Phase Transitions of Na<sub>2</sub>SO<sub>4</sub>. *J. Appl. Crystallogr.* **1996**, *29*, 42–47.
- (36) Ojima, K.; Nishihata, Y.; Sawada, A. Structure of Potassium Sulfate at Temperatures from 296 K down to 15 K. *Acta Crystallogr., Sect. B* **1995**, *51*, 287–293.
- (37) Weber, H. J.; Schulz, M.; Schmitz, S.; Granzin, J.; Siegert, H. Determination and Structural Application of Anisotropic Bond Polarizabilities in Complex Crystals. *J. Phys.: Condens. Matter* **1989**, *1*, 8543–8557.
- (38) Rentzeperis, P. J.; Soldatos, C. T. The Crystal Structure of the Anhydrous Magnesium Sulphate. *Acta Crystallogr.* **1958**, *11*, 686–688.
- (39) Weil, M. The High-Temperature Modification of Magnesium Sulfate ( $\beta$ -MgSO<sub>4</sub>) from Single-Crystal Data. *Acta Crystallogr., Sect. E* **2007**, *63*, i172–i174.

(40) Antao, S. M. Crystal-Structure Analysis of Four Mineral Samples of Anhydrite,  $\text{CaSO}_4$ , Using Synchrotron High-Resolution Powder X-ray Diffraction Data. *Powder Diffract.* **2011**, *26*, 326–330.

(41) Jacobsen, S. D.; Smyth, J. R.; Swope, R. J.; Downs, R. T. Rigid-Body Character of the  $\text{SO}_4$  Groups in Celestine, Anglesite and Barite. *Can. Mineral.* **1998**, *36*, 1053–1060.

(42) Wildner, M.; Giester, G. Crystal Structure Refinements of Synthetic Chalcocyanite ( $\text{CuSO}_4$ ) and Zincosite ( $\text{ZnSO}_4$ ). *Mineral. Petrol.* **1988**, *39*, 201–209.

(43) Dahmen, T.; Gruehn, R. Beitrage zum Thermischen Verhalten von Sulfaten. IX. Einkristallstrukturverfeinerung der Metall(III)-sulfate  $\text{Cr}_2(\text{SO}_4)_3$  und  $\text{Al}_2(\text{SO}_4)_3$ . *Z. Kristallogr.* **1993**, *204*, 57–65.

(44) Krause, M.; Gruehn, R. Contributions on the Thermal Behaviour of Sulphates XVII.1 Single Crystal Structure Refinements of  $\text{In}_2(\text{SO}_4)_3$  and  $\text{Ga}_2(\text{SO}_4)_3$ . *Z. Kristallogr.* **1995**, *210*, 427–431.

(45) Lynton, H.; Truter, M. R. An Accurate Determination of the Crystal Structure of Potassium Pyrosulphate. *J. Chem. Soc.* **1960**, 5112–5118.

(46) Naumov, D.; Virovets, A.; Podberezskaya, N.; Novikov, P.; Politov, A. Redetermination of the Crystal Structure of Potassium Peroxodisulfate ( $\text{K}_2\text{S}_2\text{O}_8$ ). *J. Struct. Chem.* **1997**, *38*, 772–778.